Available online at www.sciencedirect.com
ScienceDirect
International Journal of Heat and Mass Transfer 50 (2007) 4581–4599
International Journal of HEAT and MASS TRANSFER
www.elsevier.com/locate/ijhmt

Influence of channel-height on heat transfer in rectangular channels with skewed ribs at different bleed conditions

Shyy Woei Chang [a,*], Tsun Lirng Yang [b,1], Rong Fung Huang [c,2], Kuei Chih Sung [b,3]

[a] Thermal Fluids Laboratory, National Kaohsiung Marine University, No. 142, Haijhuan Road, Nanzih District, Kaohsiung City 81143, Taiwan, ROC
[b] Department of Marine Engineering, National Kaohsiung Marine University, No. 142, Haijhuan Road, Nanzih District, Kaohsiung City 81143, Taiwan, ROC
[c] Department of Mechanical Engineering, National Taiwan University of Science and Technology, 43 Sec. 4 Keelung Road, Taipei 106, Taiwan, ROC

Received 22 October 2006; received in revised form 15 March 2007
Available online 25 May 2007

Abstract

An infrared imaging system is used to measure detailed distributions of local heat transfer coefficient from rectangular channels with two opposite wide walls roughened by 45° staggered ribs of twenty test cases. Nusselt number (*Nu*) contours over the ribbed surfaces are presented for five sets of channels with an identical rib-floor configuration, but different channel-heights where the complex *Nu* distributions without bleed and then with bleeds from the scanned rib-floor or from the ribbed wall opposite to the scanned rib-floor or from the smooth sidewall are analyzed to examine the synergetic effects of variable channel-heights and different bleed conditions on heat transfer. Spatially averaged heat transfer results for the entire set of test channels are generated with the thermal performance factors compared to establish the heat transfer correlations with applications to the design of coolant channels in a gas turbine blade.

Keywords: Skewed ribs; Bleed channel; Gas turbine blade cooling

1. Introduction

Gas turbine engines consume high pressure air form the compressor to cool hot blades by means of film, impingement and multi-pass channel cooling. The coolant circulates through several 180° sharp turns that connect straight rib-roughened channels with various cross sectional shapes. As the coolant circulates inside the turbine blade, the sectional shapes of coolant channels are varied, but the configuration of rib-floor is sometimes identical. Twofold of geometric variations are induced by varying the channel-heights of the rib-roughened channels, namely the channel aspect ratio and the ratio of rib-height to channel-height, which in turn modify the cooling performance. The coolant is also bled from the internal cooling passages through discrete holes in order to facilitate the external film cooling. The presence of bleed-holes modifies flow structures and boundary layers of internal coolant flows that affect local heat transfer distributions on all constituent surfaces of an internal cooling passage. Knowledge about the influences of ribs and bleed-holes on internal cooling performances for channels with different aspect ratios and rib-height to channel-height ratios is essential for turbine blade designs. A large amount of experimental studies examines the fluid flow and heat transfer in the simulated cooling passage of gas turbine blades fitted with a variety of surface ribs [1–10]. Heat transfer performances in a static channel vary with configuration and arrangement of ribs [1–7], channel sectional shape and aspect ratio [8–10]. Experimental studies examine effects of bleeding flows from

* Corresponding author. Tel.: +886 7 8100888x5216; fax: +886 5716013.
E-mail addresses: swchang@mail.nkmu.edu.tw (S.W. Chang), yang2006@mail.nkmu.edu.tw (T.L. Yang), rfhuang@mail.ntust.edu.tw (R.F. Huang), kuei@mail.nkmu.edu.tw (K.C. Sung).
[1] Tel.: +886 7 8100888x5233.
[2] Tel.: +886 2 27376488.
[3] Tel.: +886 9 19616266.

0017-9310/$ - see front matter © 2007 Elsevier Ltd. All rights reserved.
doi:10.1016/j.ijheatmasstransfer.2007.03.033

Nomenclature

d	hydraulic diameter of test channel (m)
e	rib-height (m)
f	pressure-drop coefficient $= \Delta P/(0.5\rho V_{in}^2)(d/4L)$
f_∞	friction factor evaluated from Blasius equation
H	channel-height (m)
k_f	thermal conductivity of coolant ($Wm^{-1}\,K^{-1}$)
L	length of test channel (m)
l	rib land (m)
$\dot{m}$	total coolant mass flow rate into test channel ($kg\,s^{-1}$)
$\dot{m}_{Bleed}$	total mass flow rate of coolant extraction from bleeds ($kg\,s^{-1}$)
Nu	local Nusselt number over rib-roughened surface $= qd/k_f(T_w - T_f)$
Nu_∞	Nusselt number evaluated from Dittus–Boelter correlation
$\overline{Nu}$	spatially averaged Nusselt number over rib-roughened surface
n, m	correlative coefficients
P	rib pitch (m)
P_{in}	flow entry pressure ($N\,m^{-2}$)
P_{out}	flow exit pressure ($N\,m^{-2}$)
ΔP	pressure-drop over the test channel ($N\,m^{-2}$)
q	convective heat flux ($W\,m^{-2}$)
Re	Reynolds number based on channel hydraulic diameter $= \rho V_{in} d/\mu$
T_f	fluid bulk temperature (K)
T_w	wall temperature at ribbed surface (K)
V_{in}	mean flow velocity at the immediate entrance of test section ($m\,s^{-1}$)
W	channel width (m)
X, Y	coordinates in streamwise and spanwise directions (m)

Greek symbols

α	rib attack angle (deg)
η	thermal performance factor $= [Nu/Nu_\infty]/[(C_p/f_\infty)^{1/3}]$
μ	dynamic viscosity of fluid ($kg\,s^{-1}m^{-1}$)
ρ	density of fluid ($kg\,m^{-3}$)

rib-roughened channels on internal cooling performances have not been performed to a large extent. Taslim et al. [11] studied the effects of bleed-holes on heat transfer in trapezoidal straight passages roughened by tapered ribs. Shen et al. [12] performed detailed heat transfer and shear stress measurements in a convergent duct with normal ribs and film cooling holes. Bleeds alter the typical flow field between a pair of normal ribs that reduce the extent of flow separation behind each rib. Reductions of flow recirculating regions behind the ribs along with local heat transfer enhancements in the vicinity of bleed-holes increase the spatially averaged heat transfer by about 25%. Ekkad et al. [13] studied the heat transfer in a turbulated two-pass square channel with the bleed-hole along the centerline of rib-roughened surface between each pair of ribs. Along the centerline of rib-floor with bleeds, a minor heat transfer peak immediate downstream of each bleed-hole was observed. With 20–25% of the drawing bleeds in the two-pass square channel, the regional averaged heat transfer level with bleeds is similar as that for the ribbed channel without bleeds. Thurman and Poinsatte [14] reported detailed heat transfer measurements in a triple-pass channel roughened by normal ribs with bleeds in the first passage at different bleed conditions of uniform bleed, increasing and decreasing bleed flow rates per hole and no-bleed. Chanteloup and Bölics [15] performed the detailed PIV flow measurements in a two-pass channel roughened by 45° angled ribs with bleeds in the second passage. The pressure at the outlet of the two-pass channel reported in [13] or [15] is equal to the ambient pressure. As part of the coolant flow is ejected from one side of the rib-roughened channel, the streamwise symmetrical velocity profile is unbalanced toward the bleed wall that generates a strongly asymmetrical secondary flow motion. All along the channel with bleed-holes, the baseline secondary flow cells on the bleed wall have almost disappeared with its counter-rotating secondary flow cell to be enlarged. Flow fields in the entire test channel and in the region where extraction occurs are modified by adding bleed-holes through one channel wall. As the coolant extractions from one-wall of the rib-roughened channel strongly affect the rib-induced secondary flows through the entire channel, heat transfer distributions on the remaining walls without bleeds are also subject to variations from the no-bleed condition. Variations of channel aspect ratio and the wall with bleeds for a ribbed channel are likely to affect the influences of bleed on the cooling performance over the entire channel surfaces.

The objective of present study is to perform detailed heat transfer measurements using the infrared radiometer for five sets of straight rectangular channels fitted with 45° staggered ribs on two opposite wide walls with and without bleeds. Each set of five test channels share an identical rib-floor geometry, but with five different channel-heights. Four different bleed conditions (bleeds from the scanned rib-floor, bleeds from the opposite wall of scanned rib-floor, bleeds from the smooth sidewall and no-bleed) are tested for each set of five rectangular channels that examine the combined effects of variable channel-heights and bleed conditions on heat transfer. Detailed Nusselt

number measurements and the spatially averaged heat transfer results over the scanned rib-floor at different bleed conditions are compared. The heat transfer correlation is derived and the thermal performance factors for the 20 test cases are compared to enhance the cooling knowledge of gas turbine blades with bleeds.

2. Experiment

2.1. Apparatus

The flow and data acquisition systems, heat loss and heat transfer experiments and the data reduction method

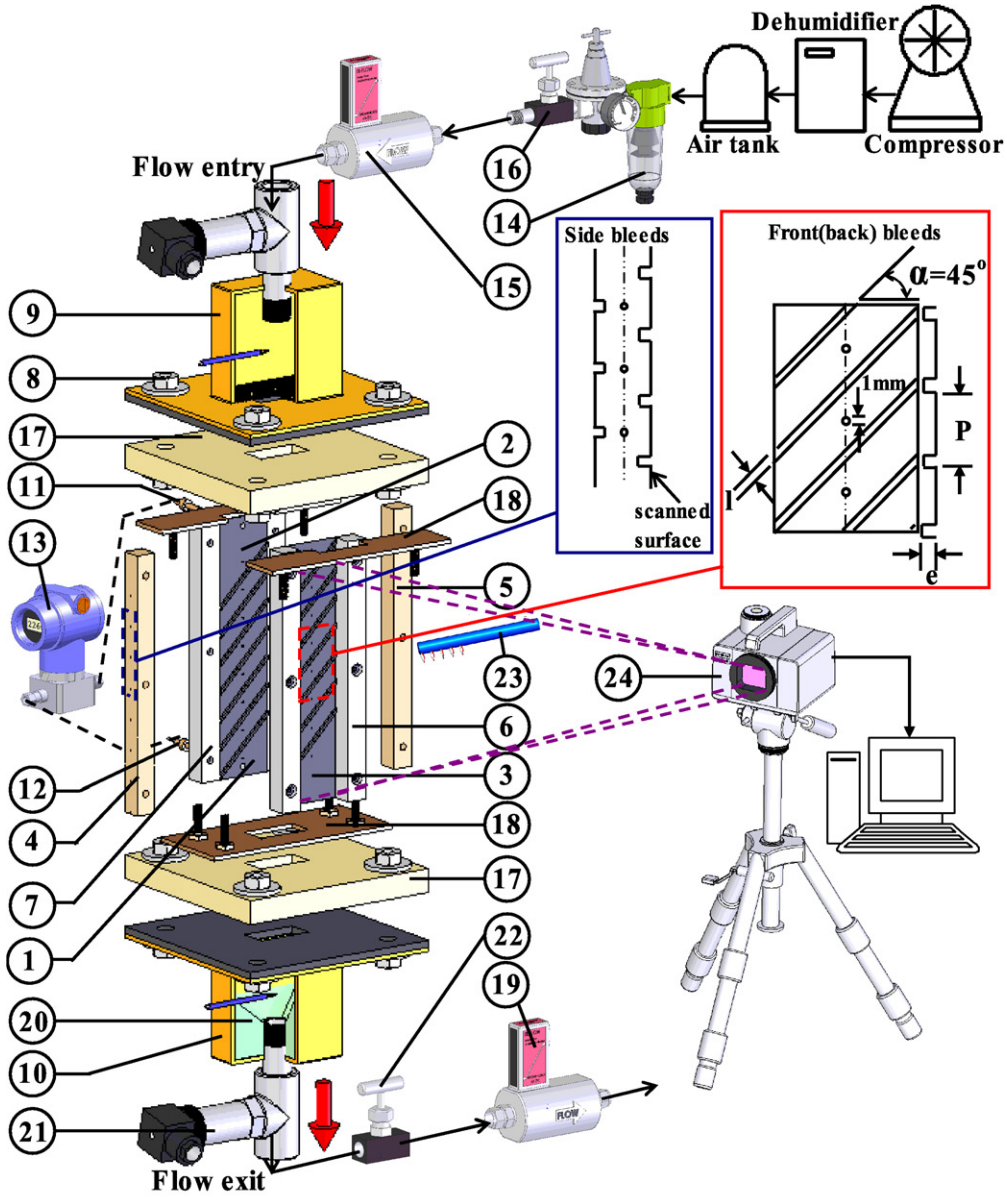

Fig. 1. Experimental apparatus.

Table 1
Geometrical specification of test channels

Rib configurations					
Rib attack angle (α) = 45° (Ribs on two opposite walls are offset by 0.5 pitch)					
Rib-height (e) = 1 mm			Rib land (l) = 1 mm		
Rib pitch (P) = 10 mm			Rib pitch to height ratio (P/e) = 10		
Width (W) (mm)	Height (H) (mm)	Hydraulic diameter (d) (mm)	Aspect ratio (H/W)	Rib-height to channel-height ratio (e/H)	Rib-height to hydraulic diameter ratio (e/d)
Test channel configurations					
40	15	22.857	0.38	0.07	0.045
40	12	16	0.3	0.08	0.05
40	9	13.33	0.23	0.11	0.07
40	6	11.43	0.15	0.17	0.09
40	4	7.272	0.1	0.25	0.14

have been previously reported [8]. Fig. 1 depicts the constructional details of the heat transfer test module. Seven pairs of square sectioned angle-ribs with the attack angle (α) of 45° at a regular interval of 10 rib-heights are arranged on two opposite wide walls of the rectangular test channel (1) in the staggered manner. Geometric features of rib and channel configurations are summarized in Table 1. Two opposite rib-roughened heating surfaces (2)(3) are made of two continuous 40 mm wide, 180 mm long and 0.1 mm thick stainless steel foils that are forged to form the rib-floor configuration. The DC electrical power is fed through two opposite heating foils (2)(3) that generate the basically uniform heat fluxes over two rib-floors. The scanned rib-roughened heating foil (2) is sandwiched between two Teflon sidewalls (4)(5) and one Teflon frame (6). Five sets of Teflon sidewalls (4)(5) with different channel-heights provide five channel aspect ratios of 0.38, 0.3, 0.23, 0.15 and 0.1. Variations of channel-height simultaneously change the channel aspect ratio and the channel-height to rib-height ratio. Another rib-shaped heating foil (3) is attached on the inner surface of a 20 mm thick Teflon back-wall (7). The complete set of test section is tightened by four draw bolts (8) between two flanges of entry (9) and exit (10) plenum chambers with the identical dimension of 75 mm × 50 mm × 80 mm. The entry plenum chamber (9) joins with the ribbed channel (1) to simulate the abrupt entry condition. Through the side wall of the ribbed channel (1), two pressure taps (11)(12) are fitted at the locations adjacent to the entry and exit planes to measure the pressure-drop over the entire test channel by a digital micromanometer (13). Eight bleed-holes with the diameter of 1 mm are located in the middle positions between two adjacent ribs as indicated in Fig. 1. Allocations of bleed-holes along the centerlines of the scanned rib-floor (2), or the opposite ribbed wall of scanned surface (3) or the one sidewall (4) are, respectively referred to as the front, back and side-bleed conditions. All the bleed air flows vent to the surrounding atmosphere.

Dry and cooled airflow from the air tank is guided through a set of pressure regulator and filtering unit (14), a mass flow meter (15) and a needle valve (16) at which the mass flow rate is metered and adjusted. Prior to entering the heat transfer test section (1), the airflow enters the entry plenum chamber (9) in which the honeycomb and steel meshes are installed between its flange and the 5 mm thick Teflon plate (17). A replaceable 3 mm thick copper plate (18) is squeezed between the Teflon plate (17) and four constituent Teflon walls (4–7). Two ends of heating foils (2)(3) are sandwiched between the insulation Teflon plate (17) and the copper plate (18) that connect with copper bars to complete the electrical heating circuit. Another massflow meter (19) after the exit plenum chamber (10) measures the exit massflow rate. Airflows vent to the surrounding atmosphere after passing through 150 mm long convergent channel (20), exit massflow meter (19), pressure transducer (21) and exit valve (22). With the predefined coolant mass flow rate specified by the tested Reynolds number, controls of entry (16) and exit valves (22) ensure that the flow exit pressure is fixed at 1.35 bar. Pressures and temperatures of test coolant in the entry plenum chamber (9) are metered by another set of pressure transducer and type K thermocouple for Reynolds number evaluation. As each bleed-hole ejects airflow to ambience that incurs the accumulated massflow losses in the streamwise direction, fluid bulk temperatures of channel flow vary in a stepwise manner [14]. Having completed each steady state wall temperature scan, the 40 mm long probing tube (23) fitted with five type K thermocouples with equal interval is horizontally probing into the test channel from the 2 mm diameter probing bore through the sidewall (5) to measure the fluid temperatures at five different spanwise locations. The flow bulk temperature at the sectional plane corresponding to each bleed-hole is obtained by averaging these five temperature measurements collecting from the probing tube (23). A linear increase of fluid bulk temperature between two adjacent bleed-holes is assumed based on the basically uniform heat flux simulated. Three additional type K thermocouples are equally spaced on the exit plane of test section to measure the flow exit temperatures. Detailed temperature distributions over the scanned rib-floor are imaged by a calibrated two dimensional infrared radiometer (24). The reference fluid temperature is selected as the local fluid bulk temperature to evaluate the local Nusselt number and the temperature dependent fluid properties such as the thermal conductivity and viscosity. The characteristic length scale selected to define Re and Nu is the hydraulic diameter of test channel, which varies with the channel aspect ratio.

2.2. Program and data processing

This study acquires detailed wall temperature measurements over the scanned ribbed surface for twenty test channels with five different channel-heights at four bleed conditions with Re varying from 5000 to 20000. The entry-plane Reynolds numbers are controlled with variations within ±1% of the targeting values. The flow condi-

tions in terms of the inlet-to-outlet pressure ratio, the overall pressure-drop across the entire test channel and the massflow fraction of total extracted flow from bleed-holes are individually measured under the isothermal conditions. With heat transfer tests, heater powers are constantly adjusted to raise the scanned spot along the centerline of the scanned rib-floor to the level of 100 °C. Steady state heat transfer measurements are performed. The steady state is assumed when the variations of wall temperatures between several successive scans are less than 0.3 °C. Having satisfied the steady state assumption, the on-line infrared thermal image program is activated to record all the wall temperature measurements for subsequent data analysis. These raw measurements are converted into local Nu over the scanned rib-floor using Eq. (1).

$$Nu = qd/k_f(T_w - T_f) \quad (1)$$

in which the local convective heat flux (q) is obtained by subtracting the local heat loss flux from the total heat flux supplied. The final phase of program analyzes and correlates the spatially averaged heat transfer data. Comparisons of overall thermal performances based on the spatially averaged heat transfer data are performed for 20 test cases. The heat transfer correlation that evaluates the spatially averaged Nusselt number over the rib-floor ($\overline{Nu}$) of each rectangular channel with four different bleed conditions is devised. The maximum uncertainties of Nu and Re are evaluated following the policy of ASME on reporting the uncertainties in experimental measurements and results [16]. The major source for attributing experimental uncertainty is from the temperature measurement. Based on the repeatability calibration tests for the present infrared thermal image system, the maximum uncertainty of the temperature measurement is estimated as ±0.7 °C. The maximum uncertainties associated with the local Nusselt and Reynolds numbers are estimated as 11.3% and 6.5%, respectively.

3. Results and discussion

3.1. Flow conditions

Fig. 2 depicts the variations of inlet-to-outlet pressure ratio (P_{in}/P_{out}) and the overall pressure-drop coefficient (f) against Re for 20 test cases. The mass flow rate of total bleed ($\dot{m}_{Bleed}$) and the extracted massflow fraction ($\dot{m}_{Bleed}/\dot{m}$) at each Re tested for all the test cases are displayed in Fig. 3. $\dot{m}_{Bleed}$ is determined as the difference between the mass flow rates measured at the inlet and exit of test section. The overall pressure-drop coefficient (f) is evaluated as $\Delta P/(0.5\rho V_{in}^2)(d/4L)$, where ΔP, ρ, V_{in} and L are referred to the nomenclature section. As shown in Fig. 2 for each set of test channels with different bleed conditions, the increase of Re driven by the increase of P_{in}/P_{out} ratio causes a corresponding increase of total bleed ($\dot{m}_{Bleed}$) as seen in Fig. 3. As the channels with front and back-bleeds share the identical bleed condition, the results of P_{in}/P_{out}, $\dot{m}_{Bleed}$, f and $\dot{m}_{Bleed}/\dot{m}$ for the front and back-bleed channels with the same H/W, e/H and e/d ratios are almost identical (see Figs. 2 and 3). In Fig. 2, the P_{in}/P_{out} ratios in the no-bleed channels are consistently higher than those in the front, back and side-bleed channels due to the larger overall pressure-drops. The side-bleed channels consistently show the lowest P_{in}/P_{out} ratios among the four comparative groups in each plot of Fig. 2. As the outlet pressures of each test channel at different bleed conditions are controlled at a fixed value of 1.35 bar, the lowest P_{in}/P_{out} ratio reflects the smallest overall pressure-drop (ΔP). The no-bleed channel and the side-bleed channel, respectively, share the highest and lowest f values at each Re tested. The f value systematically increases as channel-height decreases at each bleed condition shown in Fig. 2. This is caused by the increase of rib-height to channel-height ratio (e/H) and the decrease of channel aspect ratio (H/W) due to the decrease of channel-height, which increases the pressure-drops in the narrow ribbed channels. Overall f values decrease with the increase of Re for the no-bleed channels. In the channels with front (back) and side-bleeds, f values increase as Re increases. The different f vs. Re trends displayed in Fig. 2 between channels with and without bleeds imply the modifications of flow structures from the no-bleed scenarios due to the asymmetrical bleeds from one channel wall. It is worth noting that the maximum ΔP value acquired from the entire set of pressure-drop tests is about 150 mm-H_2O that is relatively negligible in comparison with the overall pressure levels of about 1.35 bar in the test channel. Fig. 3a–e demonstrate two sets of separated data trends of $\dot{m}_{Bleed}$ versus Re in the front (back) and the side-bleed channels. The total bleeds ($\dot{m}_{Bleed}$) from either the front (back) bleed channel or the side-bleed channel increase with the increase of Re, but $\dot{m}_{Bleed}$ from the side-bleed channels are consistently higher than those counterparts of front (back) bleed channels as seen in Fig. 3a–e. The larger amount of mass flow extraction from the side-bleed channel can considerably undermine heat transfer performances. As the decrease of channel-height systematically reduces $\dot{m}_{Bleed}$ from the front, back and side-bleed channels after examining Fig. 3a–e, the modifications of flow structures in these ribbed channels triggered by decreasing channel-height also affect the coolant extraction from each bleed. However, as the mass flow rate fed into each test channel ($\dot{m}$) is increased in order to increase Re, the ratios of coolant extraction ($\dot{m}_{Bleed}/\dot{m}$) showed in Fig. 3f, g decrease with the increase of Re for each test case even if $\dot{m}_{Bleed}$ increases with Re. It is consistently shown in Fig. 3f, g that the $\dot{m}_{Bleed}/\dot{m}$ ratios systematically decrease with the decrease of channel-height in the channels with side and front (back) bleeds. As the total coolant mass flow rate fed into the test channel reduces with the decrease of channel-height in order to keep Re at a predefined value, the converged $\dot{m}_{Bleed}/\dot{m}$ ratios in the bleed channels as Re increases actually reflect the decreased coolant extraction rate ($\dot{m}_{Bleed}$) due to the decrease of channel-height.

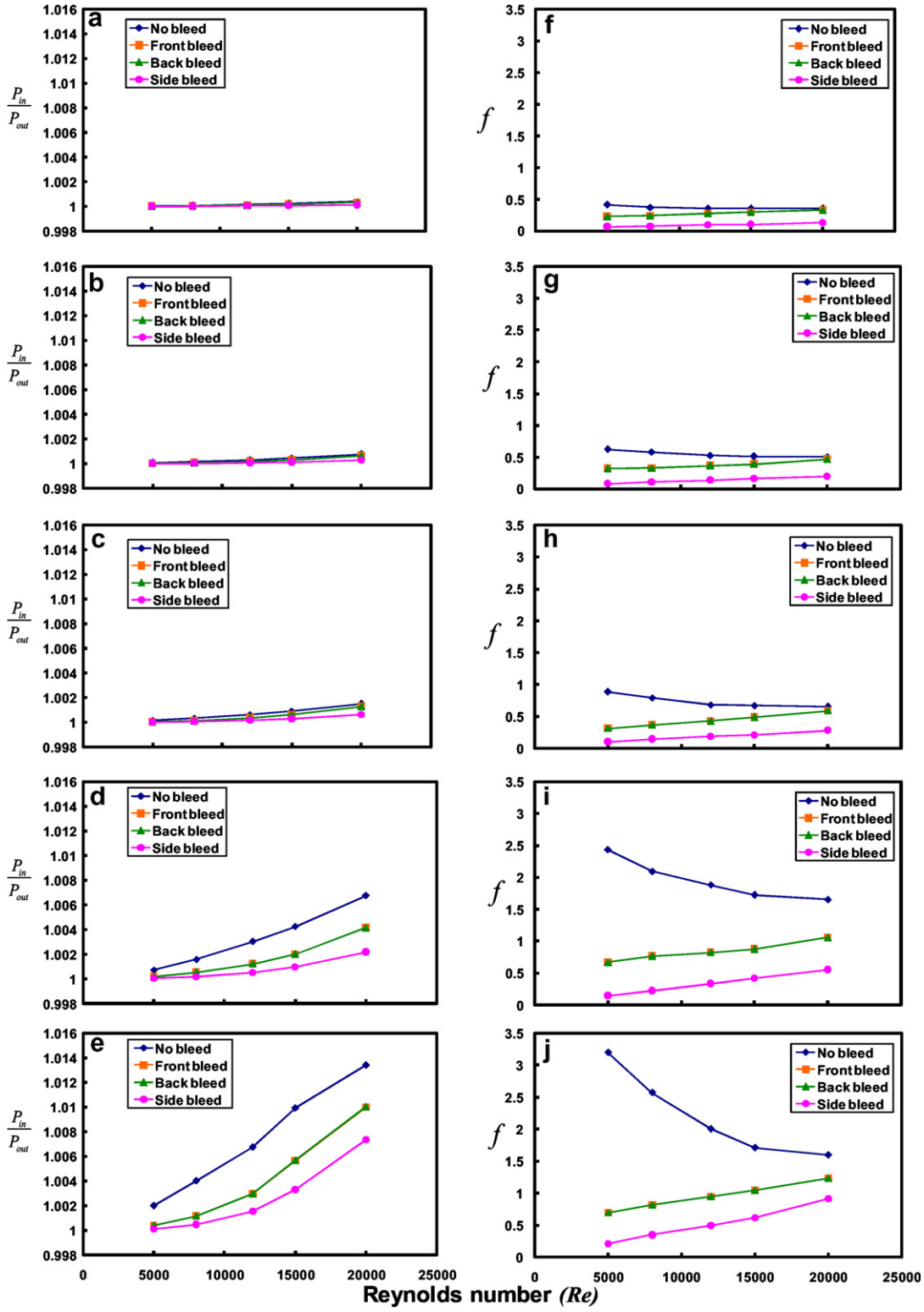

Fig. 2. Variations of inlet-to-outlet pressure ratio (P_{in}/P_{out}) and overall pressure-drop coefficient (f) against Re with (a)(f) $H/W = 0.38$ (b)(g) $H/W = 0.3$ (c)(h) $H/W = 0.23$ (d)(i) $H/W = 0.15$ (e)(j) $H/W = 0.1$ for channels with different bleed conditions.

3.2. Impacts of bleed condition on detailed Nu distributions

Figs. 4–8, respectively show the detailed Nu distributions over the rib-floors for five sets of H/W and e/H ratios at (a) no-bleed, (b) front-bleed (c) back-bleed and (d) side-bleed conditions with $Re = 20\,000$. As the channel hydraulic diameter decreases as channel-height decreases, coolant mass flow rates through the test channels compared in Figs.

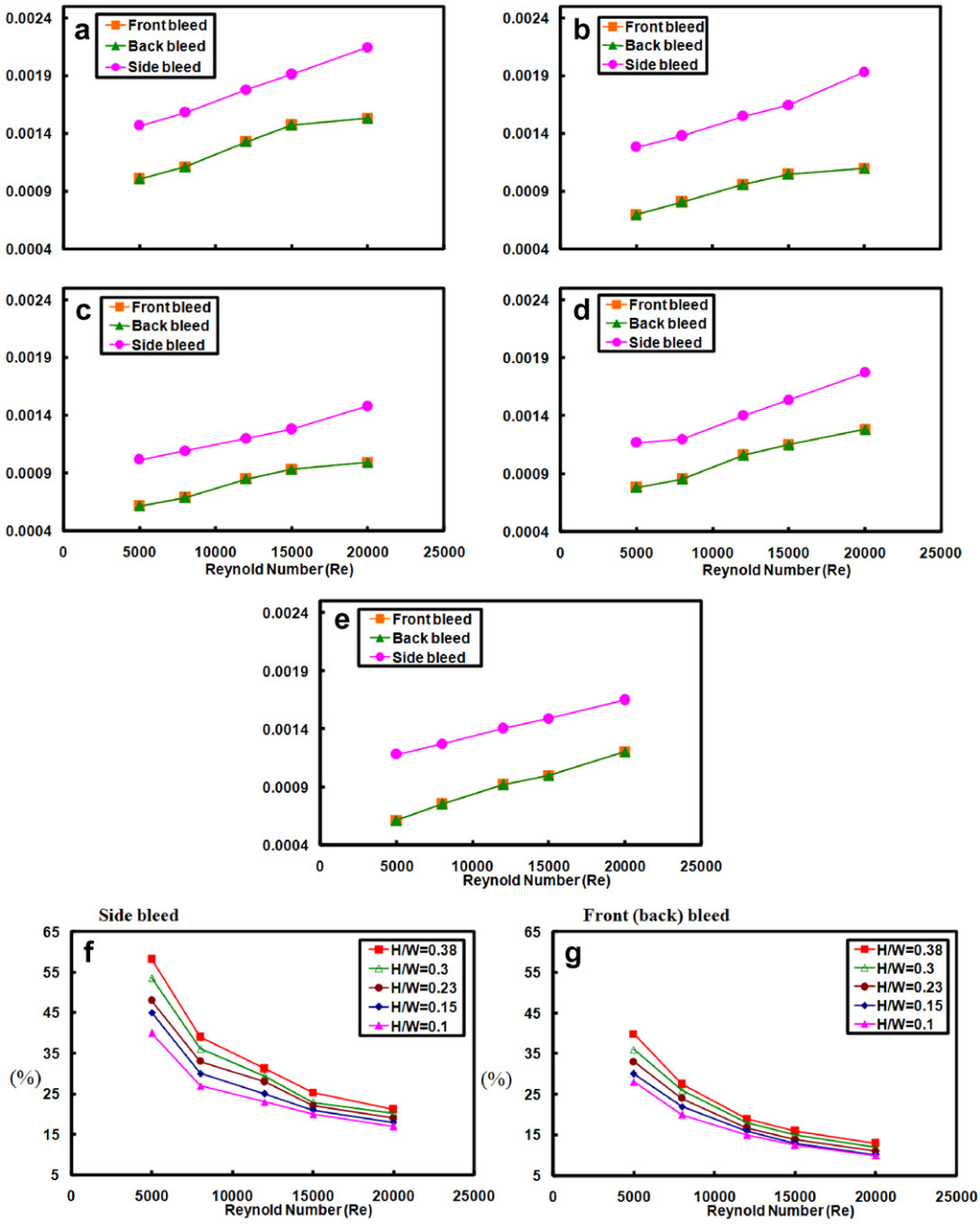

Fig. 3. Mass flow rate of total bleed ($\dot{m}_{\text{Bleed}}$) and the extracted massflow fraction ($\dot{m}_{\text{Bleed}}/\dot{m}$) at each *Re* tested with front, back and side-bleeds for all the test channels.

4–8 are systematically decreased as H/W ratios decrease from 0.38 to 0.1 in order to keep *Re* at 20000. Fig. 4 shows the *Nu* distributions at four bleed conditions with $W/H = 0.38$. In the no-bleed channel, *Nu* distributions over the rib-floor showed in Fig. 4a depict considerable streamwise and rib-wise variations. As the rib-induced secondary flows are directed in the rib-wise direction from the upper toward bottom edge of test channel, *Nu* values decrease in the rib-wise direction. Streamwise *Nu* distributions appear periodic between adjacent ribs after airflow traverses about four ribs. Each rib-top shows the regional high *Nu*. Flow separations behind ribs generate low heat transfer regions behind these angled ribs. As shown in Fig. 4a, a skewed low *Nu* band with the bandwidth about one rib-height is immediately followed behind each angled rib. Such high *Nu* on rib-tops and low *Nu* behind-ribs have been previously reported [1–10].

Effects of front-bleeds on *Nu* distributions over the rib-floor are clearly shown in Fig. 4b as the high *Nu* values around each bleed hole. There is no considerable rib-top heat transfer augmentation, but with the considerable heat transfer reduction behind each rib as shown in Fig. 4b, which is different from the high rib-top *Nu* in the no-bleed channel. An overall review of *Nu* distributions

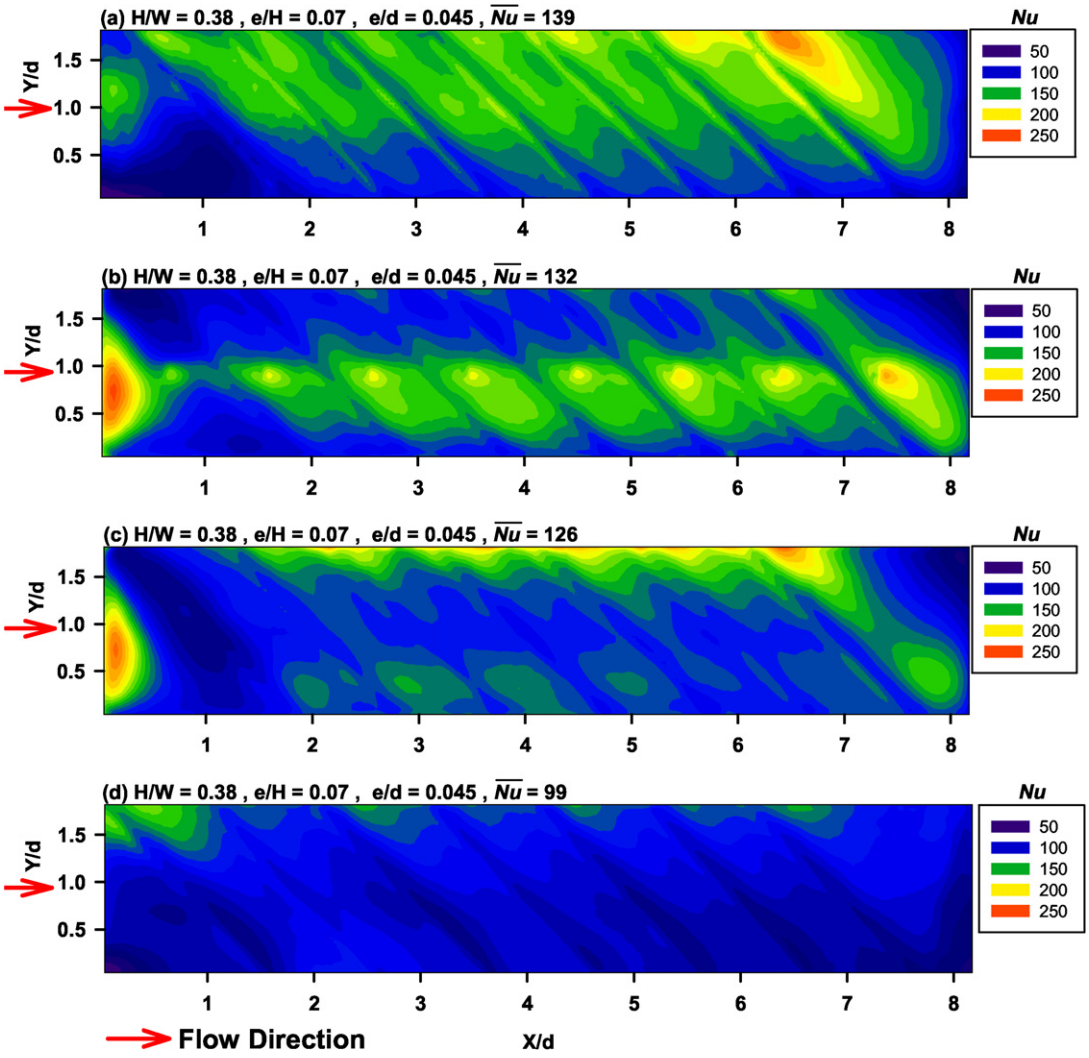

Fig. 4. Detailed heat transfer distributions over rib-roughened surfaces for channels of $H/W = 0.38$ at: (a) no-bleed, (b) front-bleed, (c) back-bleed and (d) side-bleed with Reynolds number of 20000.

with $H/W = 0.38$ at the front, back and side-bleed conditions as compared in Fig. 4b, d ensures a consistent data trend of negligible heat transfer augmentations on the rib-tops, but with considerable heat transfer reductions behind the angled ribs. The structures of secondary flows induced by angled ribs undergo considerable modifications from the no-bleed conditions after adding the bleed-holes on the front, back or side wall for such narrow channels. Referring to the flow measurements reported in [15], the secondary flow cells above the bleeding wall have almost disappeared. Rib-induced secondary flows become highly asymmetrical as the bleeds are extracted only from one ribbed wall. Strengths of the rib-induced swirls over each rib-top become relatively weak as a result of front, back or side-bleeds in the channels of $H/W = 0.38$, so that the rib-top heat transfer enhancements in the bleed channels of $H/W = 0.38$ are weakened. Further reductions of channel-height to the conditions of $H/W \leqslant 0.15$ and $e/H \geqslant 0.07$ that enhance the relative strengths of rib-induced swirls regain the high Nu values on rib-tops. Details in this respect will be discussed when the test results for the channels of $H/W \leqslant 0.15$ and $e/H \geqslant 0.07$ are presented. Also shown in Fig. 4b, neither the first bleed-hole considerably affects Nu distributions nor is the rib-wise Nu variation as evident as that shown in Fig. 4a with no-bleed in the flow region between the first and second ribs. After the second bleed hole, the front-bleeds start providing considerable impacts on rib-induced swirls. As a result, the Nu distributions between two adjacent ribs showed in Fig. 4b are considerably modified from those in the no-bleed channels. As seen in Fig. 4b with front-bleeds, a high Nu region downstream of each bleed-hole in the rib-wise direction is observed. Due to the combined effects of front-bleeds and rib-induced swirls, the shape of Nu contour around each bleed-hole follows the skewed ⟍⟋ pattern. In the narrow front-bleed channel with skewed ribs, the boundary layers surrounding each bleed-hole are essentially bled off in the rib-wise direction that enhances the regional heat transfers at locations immediate upstream and further downstream of each bleed-hole.

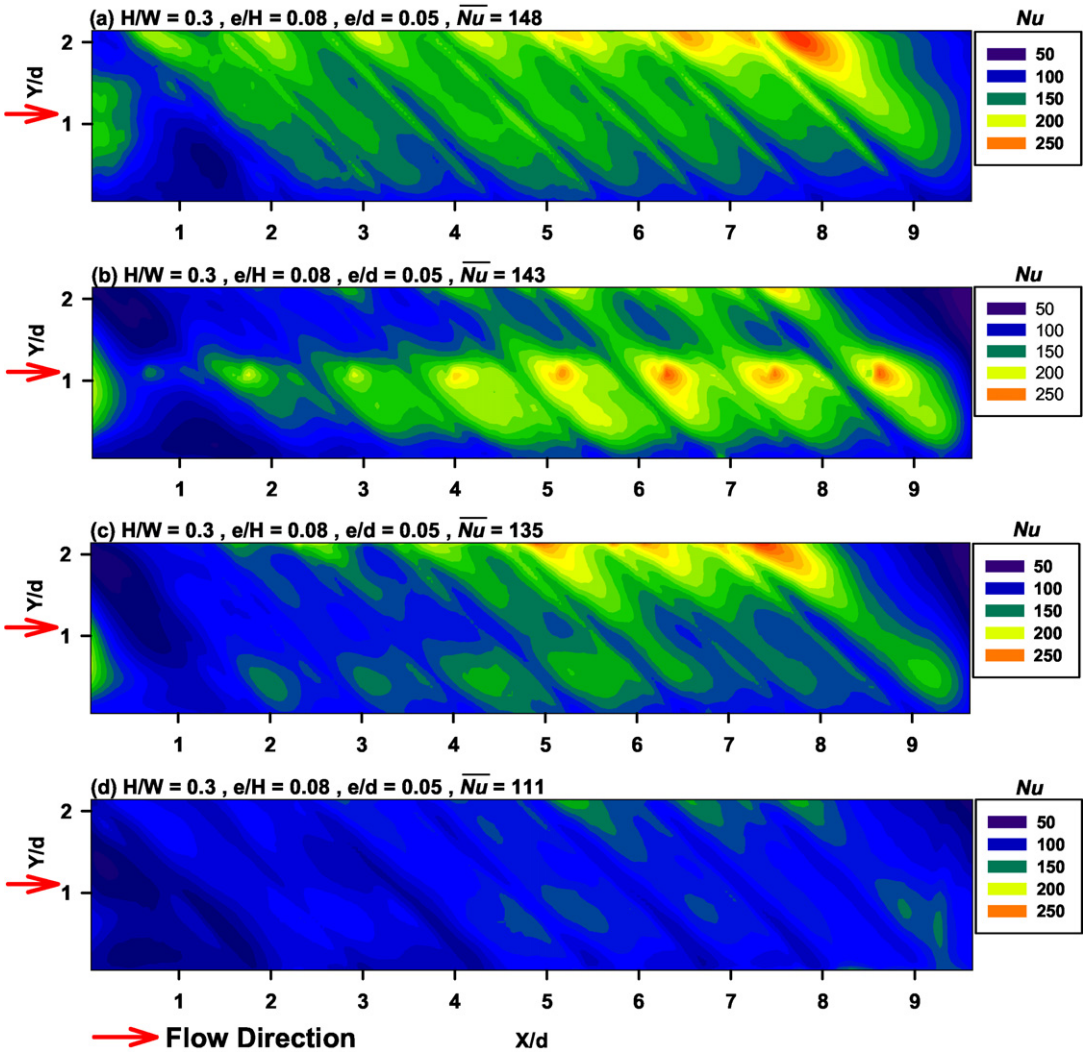

Fig. 5. Detailed heat transfer distributions over rib-roughened surfaces for channels of $H/W = 0.3$ at: (a) no-bleed, (b) front-bleed, (c) back-bleed and (d) side-bleed with Reynolds number of 20 000.

A jointed version of Fig. 4b, c is treated as the heat transfer scenarios over two opposite rib-floors with one-wall bleeds that reflects the modified secondary flow structures in the channel with one-wall bleed from ribbed floor. High *Nu* values along the upper edge of back-bleed channel in Fig. 4c correspond to the low *Nu* values along the upper edge of front-bleed channel shown in Fig. 4b. In contrast with the upper edge heat transfer scenarios depicted in Fig. 4b, c, the high *Nu* regions downstream of the bleed holes depicted in Fig. 4b correspond to the low heat transfer regions along the bottom edge of back-bleed channel showed in Fig. 4c. This interesting heat transfer behavior features the development of roll-cell vortical flows in the narrow channel with bleeds from one ribbed wall so that the cold coolant from channel core rolls toward the bleeding surface in the direction downstream of the bleed-holes. Strong rib-wise flows between two adjacent ribs direct the cold stream to wash the bleeding surface after each bleed-hole. Heated coolant streams after washing over the downstream surfaces of these bleed-holes are circulated toward its opposite wall which produces the low *Nu* values over the bottom region of back-bleed surface. Another vortical flow is induced that washes the cold coolant from the upper edge of the back-wall toward its opposite front-bleed wall. This set of roll-cells produces high *Nu* regions on the upper portion of the back-bleed channel as seen in Fig. 4c relative to the low *Nu* regions along the upper edge of front-bleed surface as shown in Fig. 4b. Cross examinations of *Nu* distributions shown in Fig. 4b, c reveal the large high *Nu* regions on the bottom portions of front-bleed surface relative to the small *Nu* regions along the upper edge of back-bleed surface. The pair of counter-rotating flow cells induced by such one-wall bleeds appears to be asymmetrical. Differences in the spatially averaged Nusselt number ($\overline{Nu}$) over the rib-floors between three test conditions compared in Fig. 4a–c are less than 8%, although the $\dot{m}_{\text{Bleed}}$ values from the front or back-bleed channels reach about 12% of the total mainstream flow. This indicates the overall heat transfer enhancements when the bleed flow only extracts from

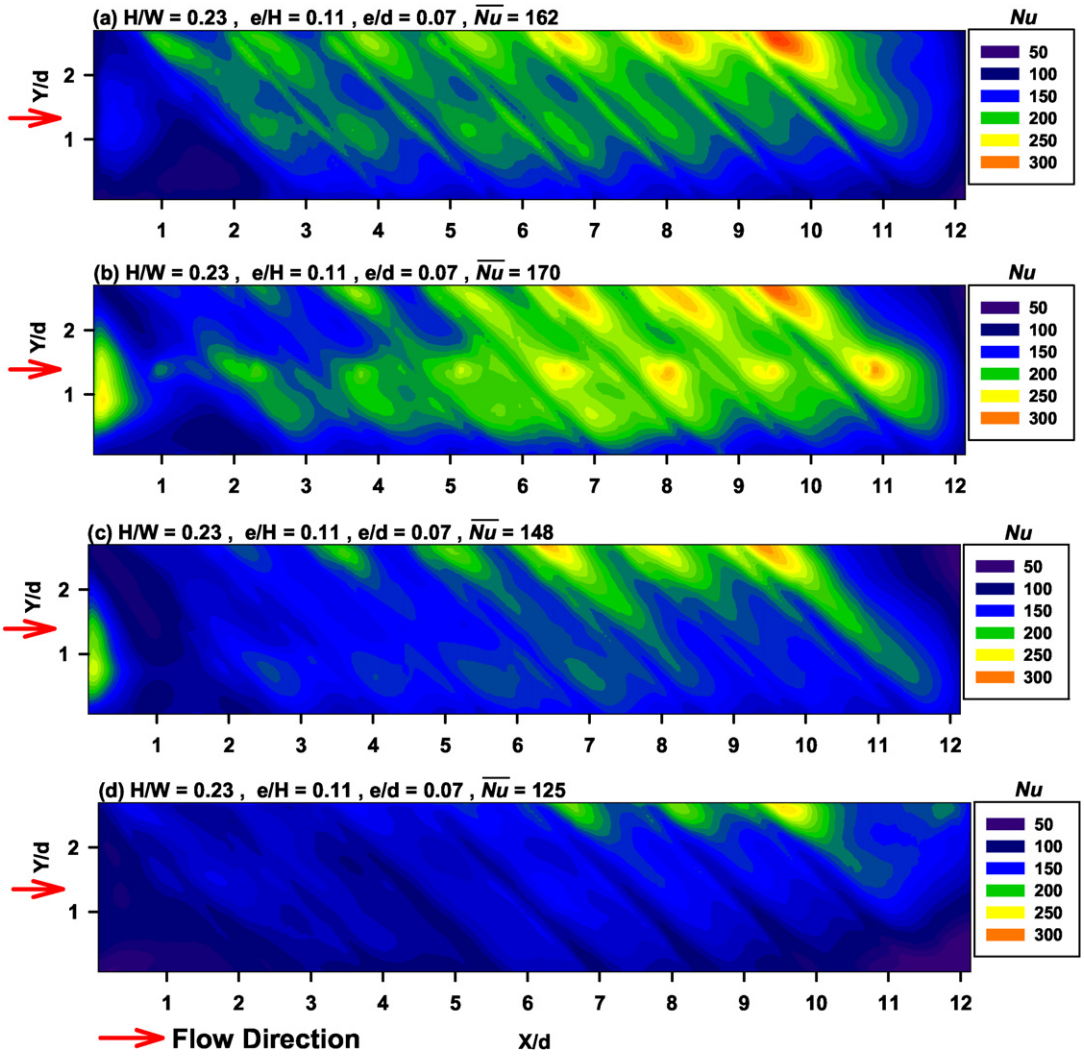

Fig. 6. Detailed heat transfer distributions over rib-roughened surfaces for channels of $H/W = 0.23$ at: (a) no-bleed, (b) front-bleed, (c) back-bleed and (d) side-bleed with Reynolds number of 20000.

one ribbed wall. Fig. 4d depicts the *Nu* distributions over the rib-floor with bleed-holes allocated at the mid-rib locations through the bottom side wall. The mass flow extraction from the side-bleeds reaches about 25% of the total mainstream flow, which is increased from the12% with front and back-bleeds. As shown in Fig. 4d, the rib-wise *Nu* variations are evident, but the heat transfer augmentations on rib-tops are less effective than the no-bleed results. This feature the strong rib-wise flows in the side-bleed channel while the streamwise separations and reattachments are modified from the no-bleed conditions. As the bleed-holes are through the side wall, boundary layers over two rib-floors can not be bled off by side bleeds. It is also unlikely that such side-bleeds can trigger the asymmetrical vortex pair that enhances the fluid mixing. As a result, the side-bleed channel shares the similar *Nu* pattern over the rib-floor with the no-bleed case to large extents, but provides the lowest $\overline{Nu}$ vale among the four comparative cases summarized in Fig. 4.

As shown in Fig. 4, the abrupt entry condition generates high *Nu* regions adjacent to the flow entrance. Locations of entry regions with high *Nu* values vary with the bleed condition. In the no-bleed channel, the flow entry region is shifted upward from the channel centerline due to the presence of skewed ribs. In the front and back bleed channels, the entry regions are pushed downward from the channel centerline as seen in Fig. 4b, c. Due to the first bleed-hole on the bleeding wall in the flow entry region, Fig. 4b depicts the larger entry region with the higher heat transfer rates relative to its opposite entry region on the back-bleed wall as shown in Fig. 4c. Asymmetrical rib-induced secondary flows are therefore initiated from the first bleed-hole in the channel with front or back-bleeds. In the side-bleed channel, the side-bleeds affect the spanwise pressure distributions that enhance the rib-wise flows. As a result, rib-wise *Nu* variations are advanced to the first pair of skewed ribs as seen in Fig. 4d. The high heat transfer entry region is developed on the upper left corner of the side-bleed channel as a jointed venture of abrupt entrance and side-bleeds. However, afore mentioned entry effects are gradually diminished as the channel-height decreases that will be illustrated in the later sections.

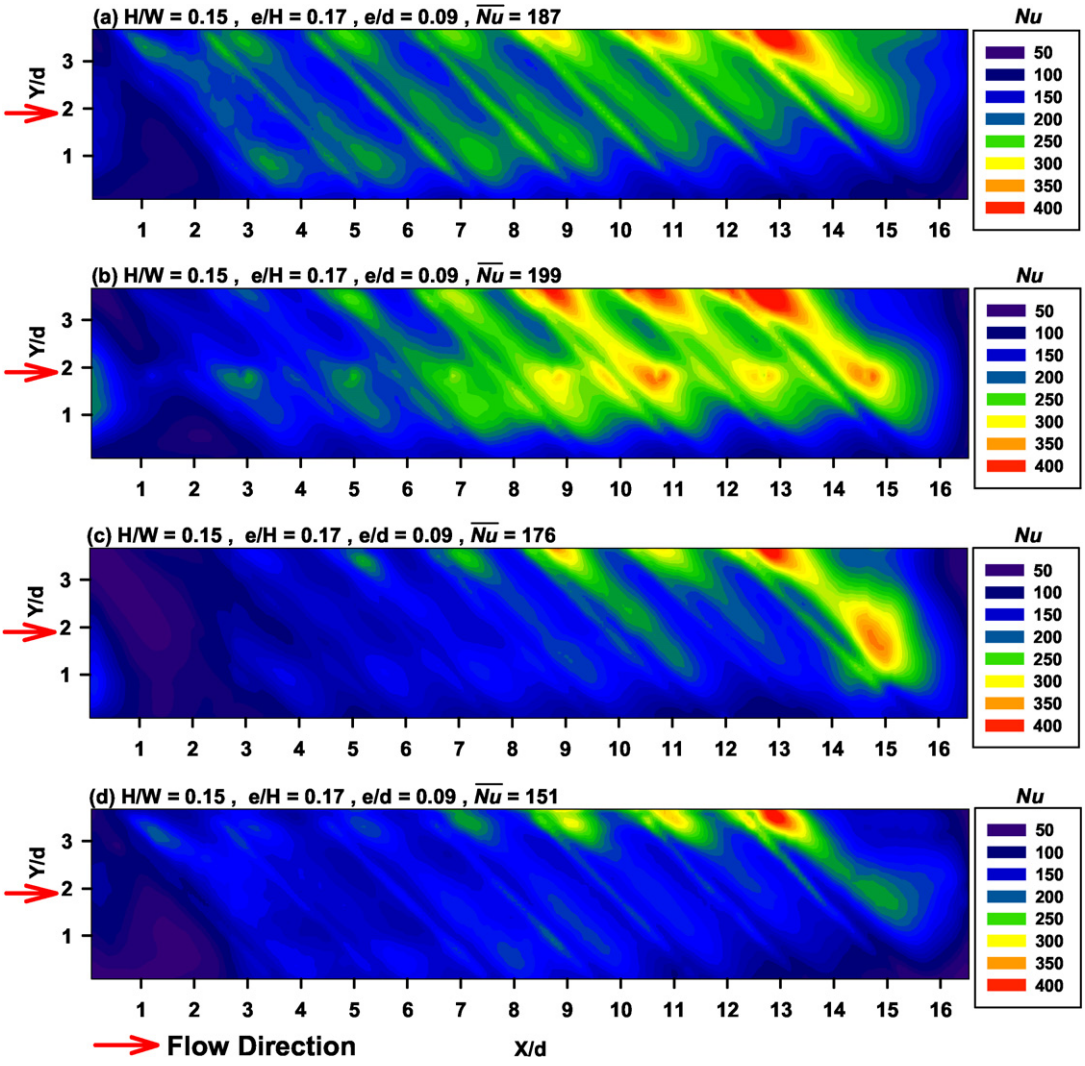

Fig. 7. Detailed heat transfer distributions over rib-roughened surfaces for channels of $H/W = 0.15$ at: (a) no-bleed, (b) front-bleed, (c) back-bleed and (d) side-bleed with Reynolds number of 20 000.

3.3. Impacts of channel-height on Nu distributions at different bleed conditions

Variations of *Nu* distribution corresponding to the decrease of channel-height that varies H/W and e/H ratios at different bleed conditions are sequentially displayed from Figs. 4–8. Behind each rib, Nusselt numbers fall radically within the bandwidth of about 0.5–1 rib-height as shown in Figs. 4–8. Such behind-rib low *Nu* regions located in the recirculation zones undergo the near-wall streamwisely reverse flows with turbulence intensities suppressed [17]. At the no-bleed condition, rib-wise *Nu* variations are accompanied with streamwise *Nu* ripples between two adjacent ribs with rib-top *Nu* peaks and the mid-rib *Nu* peaks. In the channels of $H/W = 0.38$ and 0.3, the streamwise *Nu* distributions shown in Figs. 4a and 5a follow the typical separation-and-reattachment pattern with a heat transfer bump between two adjacent ribs [1,2]. In the channels of $H/W = 0.23$, 0.15 and 0.1, the opposite wall effects trigger the mid-rib *Nu* spikes with the bandwidth about 1.5–2 rib-heights, which has led to the twin-ripple *Nu* distributions between each rib pitch. As the channel-height is reduced, the rib-floor *Nu* profiles for the no-bleed channels follow a systematic varying manner from the typical separation-and-reattachment scenarios showed in Fig. 4a to the so-called twin-ripple patterns typified by Fig. 8a. This particular heat transfer behavior is caused by the reduction of channel-height with the ribbing topology remaining fixed, which is attributed to the back-wall interaction. As seen from Figs. 4b, 5b, 6b, 7b and 8b at the front-bleed condition, the area with regional heat transfer augmentation around each bleed-hole is gradually enlarged from the downstream to the upstream of each bleed-hole as the ratios of H/W (e/H) decrease (increases) from 0.38 (0.07) to 0.1 (0.25). This particular heat transfer phenomenon due to the reduction of channel-height is typical for all the test results obtained with different *Re*. The jointed visions of *Nu* distributions in the channels of W/H (e/H) = 0.15 (0.17) and 0.1 (0.25) as seen in Figs. 7b, c and 8b,c, respectively, reveal the high regional *Nu* levels

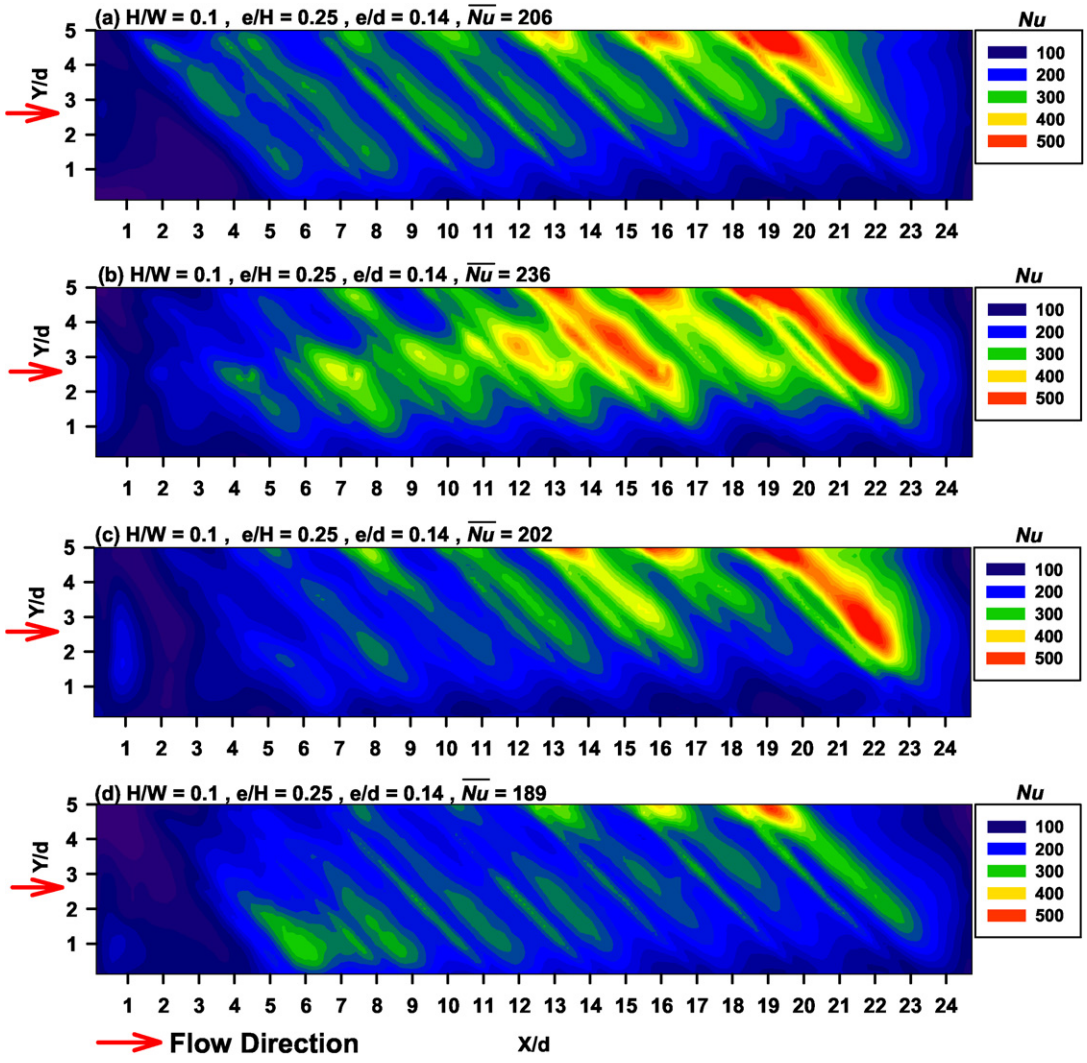

Fig. 8. Detailed heat transfer distributions over rib-roughened surfaces for channels of $H/W = 0.1$ at: (a) no-bleed, (b) front-bleed, (c) back-bleed and (d) side-bleed with Reynolds number of 20000.

among both upper portions on two opposite ribbed walls with one-wall bleeds. This implies the variation of secondary flow structures in the front or back-bleed channel as the channel-height reduces. Instead of circulating coolant from the back-bleed wall to the front-bleed wall as seen in the wider channels of Fig. 4b, c, the high heat transfer rates over the upper portions of two opposite rib-floors as seen in Fig. 7b, c and Fig. 8b, c feature the different mode of secondary flows in theses bleed channels with small heights.

The $\overline{Nu}$ ratios of font-bleed channel to the no-bleed reference for channels with different heights are examined. As marked in Figs. 4a, b, 5–7 and 8a, b, the $\overline{Nu}$ ratios between the front-bleed wall and the no-bleed reference vary from $0.95 \rightarrow 0.97 \rightarrow 1.05 \rightarrow 1.064 \rightarrow 1.15$ as the channel-height reduces. The $\overline{Nu}$ ratios between the back-bleed wall and the no-bleed reference vary from $0.906 \rightarrow 0.912 \rightarrow 0.913 \rightarrow 0.94 \rightarrow 0.98$ as the channel-height decreases as seen in Figs. 4a, c, 5–7 and 8a, c. Because the ratios of H/W, e/H and e/d for all the four test channels compared in each figure shown in Figs. 4–8 are identical, the increased front-bleed $\overline{Nu}$ values from the no-bleed $\overline{Nu}$ counterparts as shown in Figs. 7b and 8b reflect the additional flow complexities taking place inside such front-bleed channels with small heights that leads to the further heat transfer augmentation. While the $\overline{Nu}$ values at four bleed conditions collected in each figure shown in Figs. 4–8 are compared, there are 12–25% of coolant extractions from the no-bleed reference conditions. It is conjectured that the secondary flows induced by the one-wall bleeds in the square passages as reported by Chanteloup and Bölics [15] undergo the structural modifications to large extents in the narrow channels selected to acquire the heat transfer data depicted in Figs. 7b, c and 8b, c. Detailed flow measurements are requested in order to clear the heat transfer physics that are responsible for the heat transfer variations demonstrated from Figs. 4b, c, 5b, c, 6b, c, 7b, c, and 8b, c. Impacts of channel-height on Nu distributions for side-bleed channels are mainly attributed to the back-wall interactions as seen from Figs. 4d, 5d, 6d, 7d and 8d. In this respect, the relatively high heat transfer rates on the

rib-tops emerge in Figs. 7d and 8d. The high Nu spots on the upper left corner of the side-bleed channel as shown in Fig. 4d become vague in Fig. 5d and are disappeared from Figs. 6d, 7d and 8d. Degrees of similarity in Nu distributions over the rib-floors between side-bleed and no-bleed channels are gradually enhanced as the channel-height systematically decreases. The twin-ripple Nu distributing pattern between two adjacent ribs also developed in Figs. 7d and 8d for the channels with side-bleeds. As compared in Figs. 4a, d, 5–7 and 8a, d, the side-bleed to no-bleed $\overline{Nu}$ ratios increase from $0.712 \rightarrow 0.75 \rightarrow 0.77 \rightarrow 0.81 \rightarrow 0.91$ as the channel-height systematically decreases. The enhanced synergetic effects between back-wall interactions and side-wall bleeds are considered as the major attribute for the systematic increase of $\overline{Nu}$ ratios between the side and no-bleed channels. The $\overline{Nu}$ values at all bleed conditions examined consistently increase as the channel-height decreases. The previous studies concerning narrow channel flows [3,18] revealed that the rib-induced transverse flow velocities relative to the mainstream velocities are weaker than those found in square channels so that the heat transfer augmentation attributed to V-ribs in the narrow channel with $H/W = 0.125$ is less effective than the square channels [18]. The systematic elevations of $\overline{Nu}$ levels as the channel-height decreases as shown in Figs. 4–8 at all the bleed conditions tested are not attributed to the decrease of H/W ratio, but caused by the increase of e/H ratio from 0.07 to 0.25 due to the enhanced back-wall interactions and the modified secondary flows inside these rib-roughened narrow channels.

3.4. X-wise heat transfer distributions

Fig. 9 compares the X-wise distributions of Nusselt number ratio (Nu/Nu_∞) along three axes of $Y/W = 1/4$, 1/2 and 3/4 with $Re = 20000$ at different bleed conditions. The Nu_∞ reference is obtained from the Dittus–Boelter correlation [19]. Locations of ribs are marked as the vertical lines and indicated in Fig. 9. In each plot of Fig. 9, X-wise Nu/Nu_∞ distributions with different bleed conditions are compared at the same H/W, e/H and e/d ratios. Influences of channel-height on the X-wise Nu/Nu_∞ distributions at different bleed conditions are distinguished by comparing the plots collected in each column of Fig. 9. In each plot of Fig. 9, periodic Nu/Nu_∞ variations are evident, but the various bleed conditions produce different levels and distributing patterns of Nu/Nu_∞ ratio along the axes of $Y/W = 1/4$, 1/2 and 3/4. In the no-bleed case, the rib-top Nu/Nu_∞ peak is followed by a heat transfer valley behind each rib. A streamwise heat transfer recovery after each heat transfer valley is subsequently developed in the no-bleed channel for all the test conditions. In the no-bleed channels of H/W (e/H) = 0.15 (0.17) and 0.1 (0.25), the twin-spike Nu/Nu_∞ pattern between two adjacent ribs emerges due to the back-wall interactions. In the bleed channels of $W/H < 0.23$, X-wise multiple-spike Nu/Nu_∞ variations between two adjacent ribs are similarly observed. Nevertheless, for all the bleed channels with H/W ratios of 0.38 and 0.3, there is no evident rib-top Nu/Nu_∞ peak, but the clear Nu/Nu_∞ valley after each rib as shown in the plots of the first two rows of Fig. 9. The X-wise Nu/Nu_∞ distribution along the centerline of front-bleed channel is signified by a major Nu/Nu_∞ spike after each bleed-hole, where the extracted coolant bleeds off the boundary layers around the bleed hole, and a minor spike on the rib-top. In the plots of the first two rows of Fig. 9 ($H/W = 0.38$ and 0.3), bleed-induced Nu/Nu_∞ spikes in the front-bleed channels are clearly identified along the axes of $Y/W = 1/4$ and 1/2, but is not evident along the axis of $Y/W = 3/4$. Further reductions of channel-height with $W/H \leqslant 0.23$ vary the impact region of front-bleeds so that the front-bleed-induced heat transfer amplifications near the mid-rib locations become evident along three axes of $Y/W = 1/4$, 1/2 and 3/4. In the front-bleed channels of $W/H = 0.15$ and 0.1, the interesting triple Nu/Nu_∞ spikes between two adjacent ribs in the region of $5 \leqslant X/d \leqslant 20$ along the axis of $Y/W = 1/2$ are found in Fig. 9i, j. The Nu/Nu_∞ spike located after the bleed-hole is attributed to the mid-rib bleed while the additional Nu/Nu_∞ spike between the rib and the bleed-hole is likely induced by the staggered rib on the back-wall.

For all the back-bleed cases, the centerline Nu/Nu_∞ distributions near the mid-rib locations show the concave patterns in contrast to the sharp heat transfer amplifications after the bleed-holes over the frond bleed surfaces. The reattachment type heat transfer variations in the no-bleed channels are not exactly followed by the centerline heat transfer distributions in the back-bleed channels. Along the axes of $Y = 1/4$ and 3/4, the X-wise Nu/Nu_∞ variations over the ribbed surface with back-bleeds match the patterns of front-bleed channels with $H/W = 0.38$ and 0.3 as seen in Fig. 9a, b, k, l. Due to the coolant extractions form the back surface, the centerline Nu/Nu_∞ levels over the ribbed surface with back-bleeds are consistently lower than the no-bleed references. But such Nu/Nu_∞ differences between back-bleed and no-bleed channels are systematically reduced as the channel-height decreases. The different X-wise Nu/Nu_∞ distributions between the front- and back-bleed channels reconfirm the asymmetrical flow structures in the channels with bleeds from one ribbed wall. Further reductions of channel-height enhance similarities in the distributing patterns of X-wise Nu/Nu_∞ variations between the no-bleed and back-bleed cases. Typical twin-spike Nu/Nu_∞ distributions in the no-bleed narrow channels are evident in the back-bleed channels with W/H ratios of 0.15 and 0.1. The worst heat transfer scenarios found in the side-bleed channels show significant heat transfer reductions after ribs with the lowest Nu/Nu_∞ levels among four bleed conditions compared in each plot of Fig. 9. The side-bleeds cannot blow off the boundary layers over rib-floors, but further reduce the mass flux inside the coolant channel. Particular attentions to such heat transfer reductions due to side-bleeds from a narrow channel fitted with staggered angle-ribs are essential. Varying manners

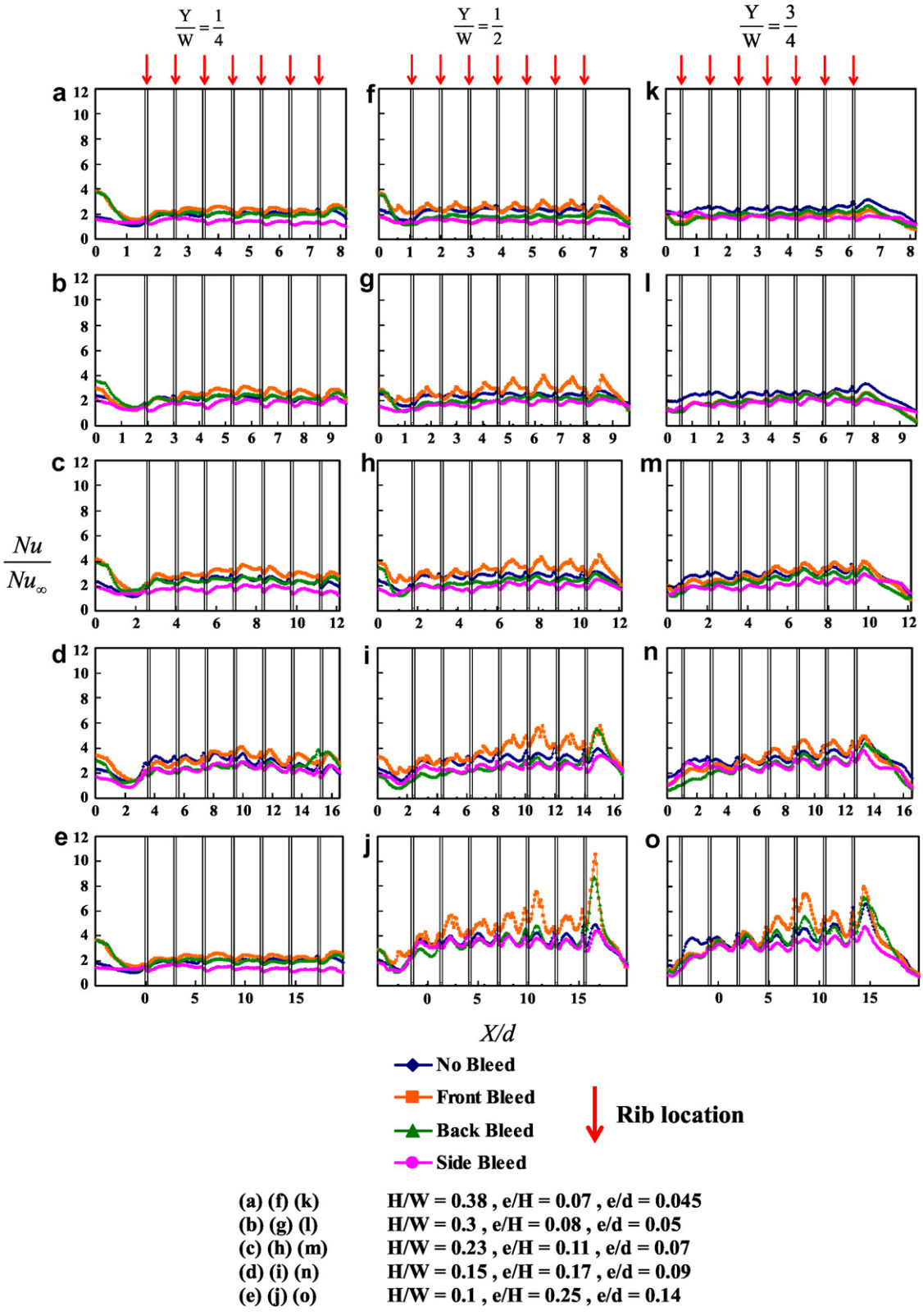

Fig. 9. X-wise distributions of Nusselt number ratio along $Y/W = 1/4$, 1/2 and 3/4 at different bleed conditions with Reynolds number of 20000.

of X-wise Nu/Nu_∞ distributions corresponding to the decrease of channel-height in side-bleed channels generally follow the data trends developed in the back-bleed channels. But due to the apparently regional heat transfer elevations along the bottom edge of ribbed surface of side bleed channel with $W/H = 0.1$ as seen in Fig. 8, the Nu/Nu_∞

ratios along the axis of $Y/W = 1/4$ for the side-bleed channel are higher than those in the channels with no-bleed and back bleeds as seen in Fig. 9e.

3.5. Y-wise heat transfer distributions

Fig. 10 compares the Y-wise Nu/Nu_∞ distributions with different bleed conditions along four spanwise axes traversing the bleed holes 1, 2, 7 and 8 over the ribbed surface at $Re = 20\,000$. The sectional Nu/Nu_∞ profiles through the bleed-holes 1 and 8 depicted in the first and forth columns of Fig. 10, respectively, traverse the upper portion of the first rib and the bottom portion of the final rib. Y-wise Nu/Nu_∞ profiles through the bleed holes 2 and 7, as depicted by the plots collected in the second and third columns of Fig. 10, pass through the upper and bottom portions of two adjacent skewed ribs. The sectional Nu/Nu_∞ profile traversing the bleed-hole 7 typifies the Y-wise heat transfer variation in the repeated flow region. Again, the influences of channel-height on Y-wise Nu/Nu_∞ distributions at different bleed conditions are revealed by comparing the plots collected in each column of Fig. 10. The

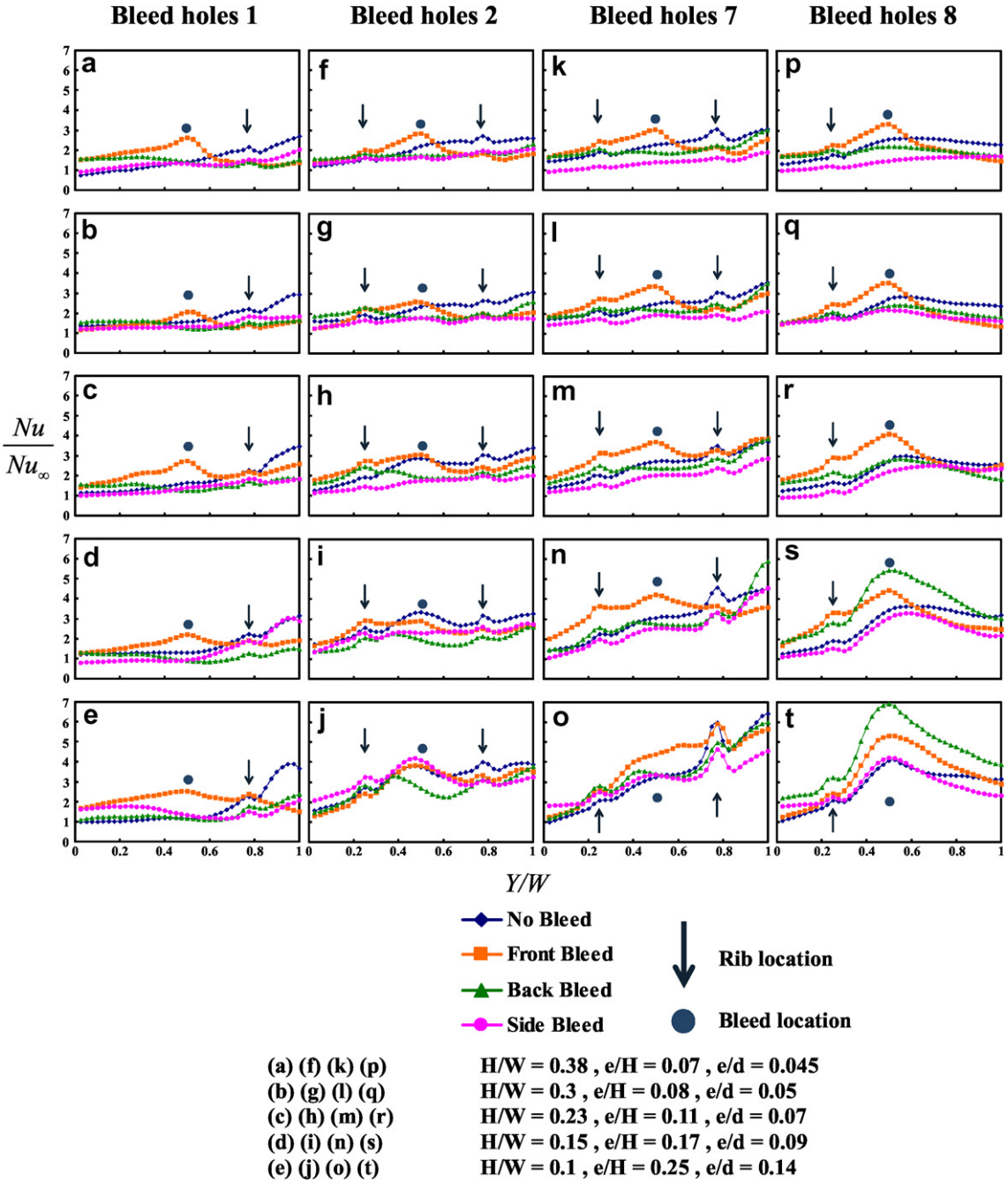

Fig. 10. Y-wise distributions of Nusselt number ratio along four spanwise axes traversing bleed-holes 1, 2, 7 and 8 at different bleed conditions with Reynolds number of 20000.

changes of Y-wise Nu/Nu_∞ profiles in the streamwise direction for the no-bleed channel with $W/H(e/H) = 0.38$ (0.07) are revealed by viewing Fig. 10a, f, k, p. These Y-wise Nu/Nu_∞ variations in no-bleed channels are generated by downwash flows in the direction along the skewed ribs so that the Nu/Nu_∞ ratios decrease from the upper edge ($Y/W = 1$) toward the bottom edge ($Y/W = 0$) as seen in Fig. 10a, f, k. After coolant traverses the final rib as indicated in Fig. 10p, the rib-wise Nu/Nu_∞ variations are weakened and reversed over the upper portion ($0.5 \leqslant Y/W \leqslant 1$) of the no-bleed channel. This particular result after the final rib in the no-bleed channel suggests that the rib-wise downwash flows vanish rapidly after the flow traverses the final pair of staggered ribs. Nu/Nu_∞ spikes in each sectional Y-wise profile of no-bleed channel are observed at the rib locations as seen in Fig. 10a, f, k, p. Such typical Y-wise Nu/Nu_∞ variations in the no-bleed channel as shown in Fig. 10a, f, k, p are similarly followed by those of no-bleed channel with $H/W(e/H) = 0.3$ (0.08), but are systematically varied as the channel-height is further reduced. The sequential variations in Nu/Nu_∞ profiles for no-bleed channels as indicated by viewing Fig. 10f–o reveal the systematically weakened Nu/Nu_∞ spikes triggered by ribs in the bottom portions of no-bleed channels as the channel-height decreases. But the rib-induced Nu/Nu_∞ spikes over the upper portion of each no-bleed channel always remain visible. An additional heat transfer bump developed in the bottom portion of $0.5 \geqslant Y/W \geqslant 0$ for the developing flows in the no-bleed channels with W/H ratios of 0.23, 0.15 and 0.1 replaces the weakened Nu/Nu_∞ spike at the bottom portion of the angled ribs as seen in Fig. 10h–j. In the very narrow no-bleed channels, such heat transfer bumps in the region of $0.5 \geqslant Y/W \geqslant 0$ with $W/H \leqslant 0.23$ as seen in Fig. 10h–j and the weakened heat transfer spikes on the bottom portion of each skewed rib are caused by the enhanced back-wall interactions.

Over the front-bleed surfaces, the Nu/Nu_∞ ratios increase in Y direction over the bottom region of $0.5 \geqslant Y/W \geqslant 0$ that reach a peak value after each bleed-hole. As a result, a heat transfer bump develops over the front-bleed surface in the bottom region of $0.5 \geqslant Y/W \geqslant 0$ that elevates the regional Nu/Nu_∞ ratios above than the no-bleed references as shown in the majority of plots collected in Fig. 10. These typical Y-wise Nu/Nu_∞ profiles over the front-bleed surfaces are consistently observed in all the plots in the first two columns and the final column of Fig. 10 over the developing and exit flow regions, respectively. The bleed-induced Nu/Nu_∞ bumps in the region of $0.5 \geqslant Y/W \geqslant 0$ after the final rib are also observed in Fig. 10p–r, but are disappeared in the front-bleed channel with the smallest channel-height as indicated in Fig. 10t. Over the bottom portions of the front-bleed channels in the region of $0.5 \geqslant Y/W \geqslant 0$, the rib-induced Nu/Nu_∞ spikes in all the sectional Y-wise profiles as shown in Fig. 10 are either weakened or vanished. The sectional Nu/Nu_∞ profiles over the front-bleed surfaces in the region of $1 \geqslant Y/W \geqslant 0.5$, which corresponds to the upstream locations of the bleed-hole in the rib-wise direction, exhibit the spanwisely concave shape in contrast to the spanwise heat transfer increases over the upper portions of no-bleed channels as seen in Fig. 10a, f, k, p and Fig. 10b, g, l, q. Variations of Nu/Nu_∞ profiles for the front-bleed channels in corresponding to the decrease of channel-height as compared by the plots of the third column in Fig. 10 that feature the heat transfer in repeated-rib region are noted. The front-bleed dominant sectional Nu/Nu_∞ profiles gradually yield into the rib-dominant profiles featured by the weakened bleed-induced Nu/Nu_∞ bump and the evident rib-induced Nu/Nu_∞ spike over the bottom portion indicated in Fig. 10m–o. Because the coolant extraction keeps bleeding off the boundary layers around each bleed-hole, the Nu/Nu_∞ ratios for the front-bleed channel in the bottom region of $0.5 \geqslant Y/W \geqslant 0$ are still higher than the no-bleed references even if the rib associated heat transfer characteristics become dominant in such narrow channels with $W/H \leqslant 0.23$.

For the back-bleed channels, neither the rib-induced Y-wise Nu/Nu_∞ variations nor the bleed-induced heat transfer bump are depicted in the sectional Nu/Nu_∞ profiles traversing the first rib and the first bleed-hole as shown in all the plots collected in the first column of Fig. 10. Rib-induced downwash flows are not properly initiated in the flow region upstream of the first bleed-hole so that the Nu/Nu_∞ spike at each rib-top is not seen for the back-bleed channels in all the plots collected in the first column of Fig. 10. Coolant extractions from the opposite bleeding surface considerably reduce Nu/Nu_∞ ratios over the developing region for back-bleed cases. In contrast to the heat transfer bump in the front-bleed channel, the Nu/Nu_∞ profile traversing the first bleed-hole in each back-bleed channel exhibits the concave shape for all the channel-heights examined as shown in the plots collected in the first column of Fig. 10. It is also noticed that the downstream variations of Nu/Nu_∞ profiles in the back bleed channels show considerable dependence on the channel-height. As the bulk flow travels in the downstream direction, the sectional Nu/Nu_∞ profiles for the back-bleed channel with $W/H = 0.38$ gradually yield into the patterns developed in the no-bleed channels as seen from Fig. 10a, f, k, p. There is no sign of development for the bleed-induced heat transfer bump in the sectional Nu/Nu_∞ profiles for the back-bleed channel with $W/H = 0.38$ as shown in plots collected in the first row of Fig. 10. But with $W/H \leqslant 0.23$, the downstream variations of Nu/Nu_∞ profiles in the back-bleed channels gradually match those of front-bleed cases as seen in the plots collected in the third, forth and fifth rows of Fig. 10. The bleed-induced heat transfer bump is similarly generated in the back-bleed channels with $W/H \leqslant 0.23$. Particularly, the Nu/Nu_∞ bumps around bleed-hole 8 in back-bleed channels of $W/H = 0.15$ and 0.1, which elevate the regional Nu/Nu_∞ ratios to be above than the front-bleed counterparts, are found in Fig. 10s, t.

The downstream developments of Y-wise Nu/Nu_∞ profiles as well as the shapes of sectional Nu/Nu_∞ profiles in

the side bleed channels generally follow the patterns observed in the no-bleed channels. In comparison with the results acquired from the no-bleed channels, the developments of Nu/Nu_∞ spikes over the bottom portions of skewed ribs in the side-bleed channels require the longer Y-wise length and the smaller channel-height. The rib-top Nu/Nu_∞ spikes in side-bleed channels are relatively weak in comparison with those developed on the rib-tops of no-bleed channels. The loss of mass flux from the bottom side wall certainly weakens the local flow momentum that transverses each angled rib. As a result, the Nu/Nu_∞ spikes on the bottom portions of skewed ribs showed in the sectional Nu/Nu_∞ profiles of Fig. 10 for the side-bleed channels are either diminished or considerably weakened. As the side-bleeds can neither considerably modify the secondary flow structures in the ribbed channel nor bleed off the boundary layers over the ribbed surface, such side-bleeds provide the lowest Nu/Nu_∞ levels in the plots collected in Fig. 10, except in the channels of $W/H = 0.15$ and 0.1. Due to the interactions between the bleed flows entry flow, the Nu/Nu_∞ ratios in the developing flow region of side-bleed channels as depicted in Fig. 10d, e, i, j are higher than the counterparts developed in the back-bleed channels.

3.6. Heat transfer correlations

The procedures of deriving $\overline{Nu}$ correlation for 20 test cases start from plotting the varying manners of $\overline{Nu}$ against Re as illustrated in Fig. 11. As compared in Fig. 11a, b, the $\overline{Nu}$ levels in the channels of $H/W = 0.38$ and 0.3 follow the order of $\overline{Nu}_{\text{no-bleed}} > \overline{Nu}_{\text{front-bleed}} > \overline{Nu}_{\text{back-bleed}} > \overline{Nu}_{\text{side-bleed}}$. A further reduction of channel-height that brings $H/W \leqslant 0.23$ modifies the varying manner of $\overline{Nu}$ against the bleed condition that gives $\overline{Nu}_{\text{front-bleed}} > \overline{Nu}_{\text{no-bleed}} > \overline{Nu}_{\text{back-bleed}} > \overline{Nu}_{\text{side-bleed}}$ as seen in Fig. 11c–e. Each data trend collected in Fig. 11 is curve fitted correlation in satisfying the condition of $\overline{Nu} \to 0$ as $Re \to 0$.

$$\overline{Nu} = mRe^n \tag{2}$$

Table 2 summarizes the correlative coefficients m and n obtained in five test channels with different bleed conditions. Maximum discrepancies between the correlated results from Eq. (2) and the experimental measurements are within $\pm 10\%$ for the entire set of $\overline{Nu}$ data generated. The exponent n depicted in Table 2 increases as the channel-height decreases. Accompanying with the increased n exponent as H/W ratio decreases is the decreased m coefficient when the channel-height decreases.

The assessment of thermal performances for all the test cases is performed by comparing the thermal performance factors of each test channel (η) defined as

$$\eta = [\overline{Nu}/Nu_\infty]/[(f/f_\infty)^{1/3}] \tag{3}$$

The friction factor (f_∞) in Eq. (3) is evaluated from the Blasius equation for turbulent flow as $0.079Re^{-0.25}$. Variations of thermal performance factor (η) with Re are compared in Fig. 12 for different test cases. In the channels of

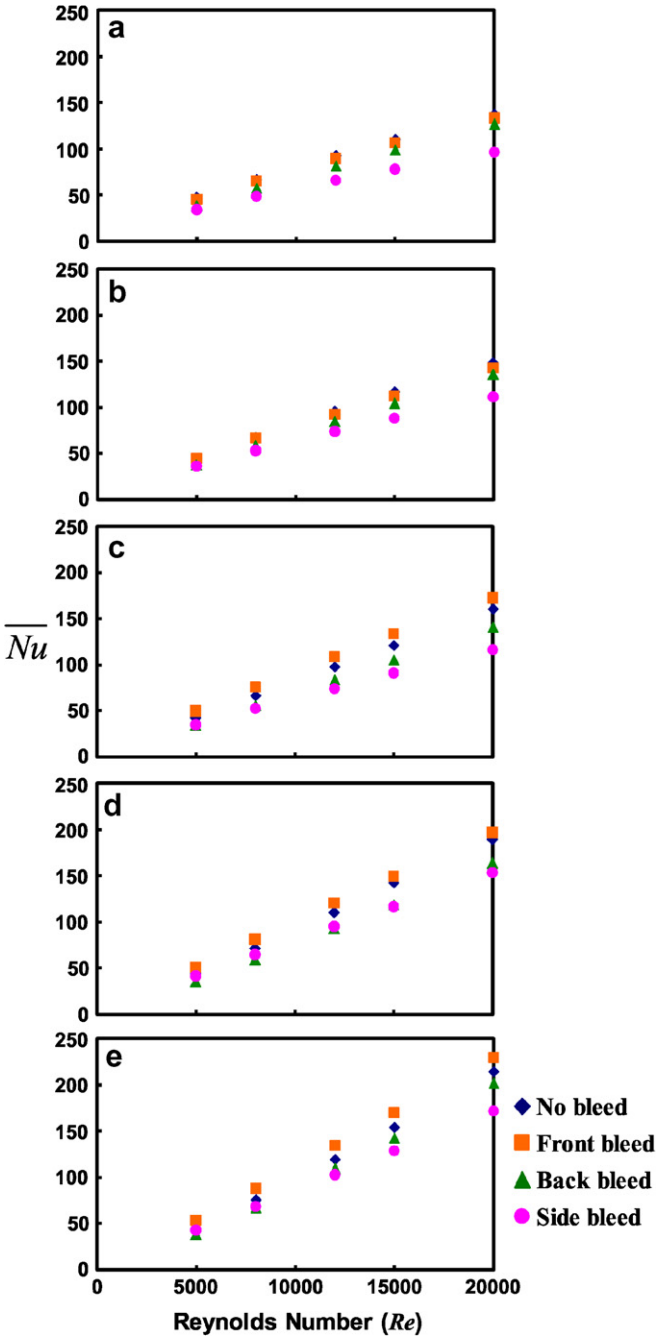

Fig. 11. Variations of $\overline{Nu}$ against Reynolds number with no-bleed, front, back and side-bleeds in channels of: (a) $H/W = 0.38$, $e/H = 0.07$, $e/d = 0.045$, (b) $H/W = 0.3$, $e/H = 0.08$, $e/d = 0.05$, (c) $H/W = 0.23$, $e/H = 0.11$, $e/d = 0.07$, (d) $H/W = 0.15$, $e/H = 0.17$, $e/d = 0.09$ and (e) $H/W = 0.1$, $e/H = 0.25$, $e/d = 0.14$.

$H/W = 0.38$, thermal performance factors obtained at all bleed conditions decrease with the increase of Re. Reductions of channel-height can reverse the varying trend of η vs. Re, but the H/W (e/H) ratios at which the reversing trend of η vs. Re relationship develop vary with the bleed condition. As indicated in Fig. 12a–d, the η values start to increase with the increase of Re as H/W (e/H) ratios become 0.3 (0.08), 0.23 (0.11) and 0.15 (0.17) for the channels with no-bleed, back-bleed and front-bleed, respectively.

Table 2
Correlative coefficients m and n in five test channels with no-bleed, front, back and side-bleeds

H/W	e/H	e/d	$\overline{Nu} = mRe^n$							
			m				n			
			No-bleed	Front-bleed	Back-bleed	Side-bleed	No-bleed	Front-bleed	Back-bleed	Side-bleed
0.38	0.07	0.045	0.0658	0.0587	0.0253	0.0573	0.772	0.78	0.86	0.75
0.3	0.08	0.05	0.0298	0.0342	0.0136	0.0365	0.8596	0.8417	0.93	0.81
0.23	0.11	0.07	0.0118	0.0235	0.006	0.0213	0.9605	0.8989	1.0172	0.8689
0.15	0.17	0.09	0.0055	0.0129	0.0035	0.0134	1.0547	0.9726	1.085	0.9432
0.1	0.25	0.14	0.0022	0.0071	0.0028	0.0082	1.1628	1.0483	1.1269	1.0044

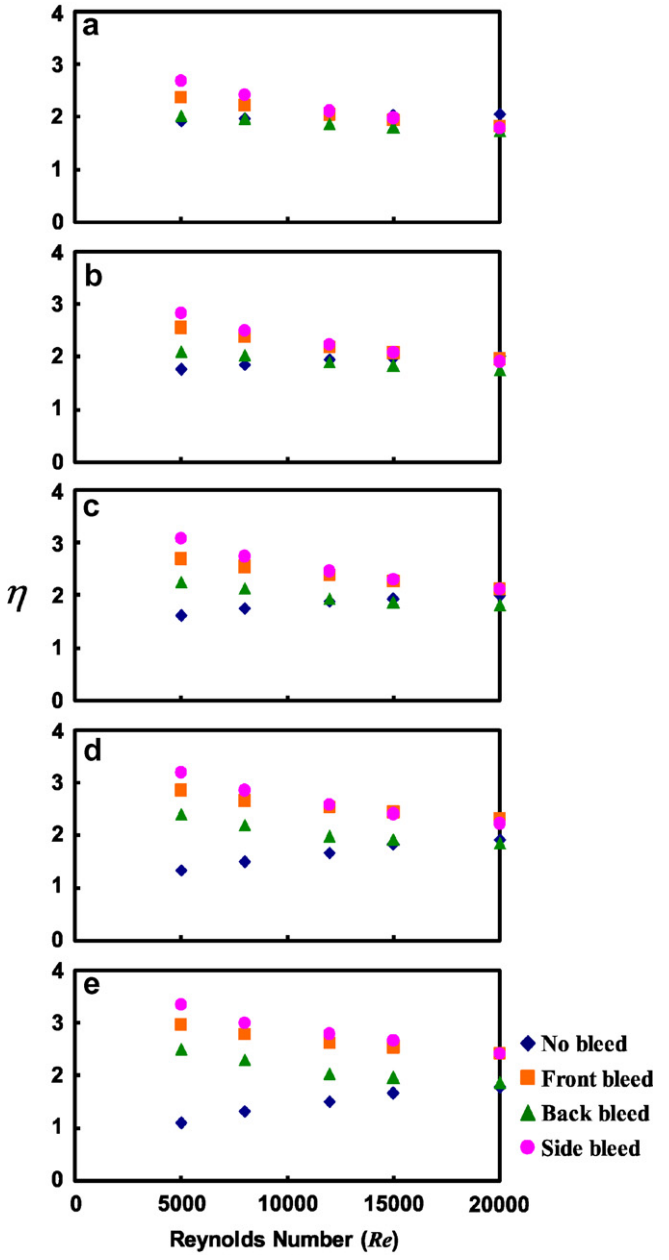

Fig. 12. Variations of thermal performance factor against Reynolds number with no-bleed, front, back and side-bleeds in channels of: (a) $H/W = 0.38$, $e/H = 0.07$, $e/d = 0.045$, (b) $H/W = 0.3$, $e/H = 0.08$, $e/d = 0.05$, (c) $H/W = 0.23$, $e/H = 0.11$, $e/d = 0.07$, (d) $H/W = 0.15$, $e/H = 0.17$, $e/d = 0.09$ and (e) $H/W = 0.1$, $e/H = 0.25$, $e/d = 0.14$.

Varying manners of η vs. Re for all the side bleed channels remain to be decreased as Re increases. In the channels with front and side-bleeds, the thermal performance factors generally increase with the decrease of channel-height. But the η values for the channels with no-bleed and back-bleeds tend to decrease with the decrease of channel-height. At each Re tested with the same channel-height, η values generally follow the order of $\eta_{\text{side-bleed}} > \eta_{\text{front-bleed}} > \eta_{\text{back-bleed}} > \eta_{\text{no-bleed}}$ as compared in each plot of Fig. 12. Although the $\eta_{\text{side-bleed}}$ is the highest among the comparative groups, precautions in the design stage for a coolant passage in a gas turbine blade with side-bleeds are required due to the lowest heat transfer coefficients.

4. Conclusions

1. Heat transfer results in no-bleed channels reconfirm the typical rib effects. The rib-induced secondary flows become asymmetrical as the bleeds are extracted from one channel wall so that the regional heat transfer enhancements on rib-tops in the channels with one-wall bleeds are weakened in the test channels of $H/W \geqslant 0.3$. Further reductions of channel-height to the conditions of $H/W \leqslant 0.15$ enhance the relative strengths of rib-induced swirls that recover the high heat transfer coefficients on rib-tops for the bleed channels.
2. Due to the combined effects of front-bleeds and rib-induced swirls, a high heat transfer region is generated immediately downstream of each bleed-hole in the rib-wise direction. Developments of rib-wise roll-cell vortical flows between two adjacent angled ribs in the channels with bleeds from one ribbed wall generate the contrasting regional heat transfer performances over the upper and bottom portions of two opposite ribbed walls with front and back-bleeds. As the boundary layers over the rib-floor can not be bled off by side-bleeds, the side bleed channels share the similar patterns of Nu distributions over the ribbed surface with the no-bleed scenarios to large extents, but provide the lowest heat transfer levels among the four comparative groups with different bleed conditions due to the loss of coolant mass flux from the side-bleeds.
3. As the channel-height is gradually reduced, variations of Nu on the rib-floor for the no-bleed case follow a systematically manner from the typical separation-and-

reattachment scenarios to the so-called twin-ripple patterns within each rib pitch. Such heat transfer behavior is mainly attributed to the back-wall interaction which also affects the impact of bleeds on heat transfer. For cases of $H/W = 0.23$, 0.15 and 0.1 ($e/H = 0.11$, 0.17 and 0.25) with and without bleeds, the opposite wall effects emerge to trigger the mid-rib *Nu* spikes, which has led to the multiple-ripple *Nu* distributions between two adjacent ribs. Spatially averaged Nusselt numbers ($\overline{Nu}$) at all bleed conditions examined are accordingly increased as the channel-height decreases. Degrees of similarity in *Nu* distributions over the rib-roughened surfaces between the channels with and without bleeds are gradually enhanced as the channel-height decreases.

4. The proposed $\overline{Nu}$ correlation shows the effect of *Re* on spatially averaged heat transfer over the rib-floors with different bleed conditions and channel-heights.
5. Thermal performance factors for the side-bleed channels consistently decrease as *Re* increases. Adjustments of channel-height can vary the η vs. *Re* relationships in the channels with no-bleed, front-bleeds and back-bleeds. The H/W (e/H) ratios at which the reversing trend of η vs. *Re* initiate vary with the bleed condition. Thermal performance factors that increase as *Re* increases for the channels with no-bleed, back and front-bleeds are observed at the H/W (e/H) ratios of 0.3 (0.08), 0.23 (0.11) and 0.15 (0.17), respectively. With any tested channel configurations at each *Re* examined, η values generally follow the order of $\eta_{\text{side-bleed}} > \eta_{\text{front-bleed}} > \eta_{\text{back-bleed}} > \eta_{\text{no-bleed}}$. However, as the heat transfer performances in the side-bleed channels are considerably undermined from the no-bleed references, precautions in the design stage for the coolant channel with side-bleeds are necessary in order to prevent the overheating situations.

References

[1] J.C. Han, Y.M. Zhang, C.P. Lee, Augmented heat transfer in square channels with parallel crossed and V-shaped angled ribs, ASME J. Turbomach. 113 (1991) 590–597.

[2] M.E. Taslim, T. Li, D. Kercher, Experimental heat transfer and friction in channels roughened with angle V-shaped and discrete ribs on two opposite walls, ASME J. Turbomach. 118 (1996) 20–28.

[3] X. Gao, B. Sundén, PIV measurement of the flow field in rectangular ducts with 60° parallel, crossed and V-shaped ribs, Exp. Therm. Fluid Sci. 28 (2004) 639–653.

[4] H.H. Cho, S.J. Wu, H.J. Kwon, Local heat/mass transfer measurement in a rectangular duct with discrete ribs, ASME J. Turbomach. 122 (2000) 579–586.

[5] T.-M. Liou, C.-C. Chen, T.-W. Tsai, Heat transfer and fluid flow in a square duct with 12 different shaped vortex generators, ASME J. Heat Transfer 122 (2000) 327–335.

[6] S. Mochizuki, A. Murata, M. Fukunga, Effect of rib arrangements on pressure-drop and heat transfer in a rib-roughened channel with a sharp 180 deg turn, ASME J. Turbomach. 119 (1997) 610–616.

[7] G. Tanda, Heat transfer in rectangular channels with transverse and V-shaped broken ribs, Int. J. Heat Mass Transfer 47 (2004) 229–243.

[8] S.W. Chang, T.-M. Liou, W.-J. Juan, Influence of channel-height on heat transfer augmentation in rectangular channels with two opposite rib-roughened walls, Int. J. Heat Mass Transfer 48 (2005) 2806–2813.

[9] J.C. Han, S. Ou, J.S. Park, C.K. Lei, Augmented heat transfer in rectangular channels of narrow aspect ratios with rib turbulators, Int. J. Heat Mass Transfer 32 (1989) 1619–1630.

[10] J.S. Park, J.C. Han, Y. Hung, S. Ou, Heat transfer performance comparisons of five different rectangular channels with parallel angled ribs, Int. J. Heat Mass Transfer 35 (1992) 2891–2903.

[11] M.E. Taslim, T. Li, S.D. Spring, Experimental study of the effects of bleed-holes on heat transfer and pressure-drop in trapezoidal passages with tapered turbulators, ASME J. Turbomach. 117 (1995) 281–289.

[12] J.R. Shen, Z. Wang, P. Ireland, T.V. Jones, A.R. Byerley, Heat transfer enhancement with a turbine blade cooling passage using ribs and combinations of ribs with film cooling holes, ASME J. Turbomach. 118 (1996) 428–434.

[13] S.V. Ekkad, Y. Hung, J.C. Han, Detailed heat transfer distributions in two-pass square channels with rib turbulators and bleed-holes, Int. J. Heat Mass Transfer 41 (1998) 3781–3791.

[14] D. Thurman, P. Poinsatte, Experimental heat transfer and bulk air temperature measurements for a multi-pass internal cooling model with ribs and bleed, ASME J. Turbomach. 123 (2001) 90–96.

[15] D. Chanteloup, A. Bölics, Flow characteristics in two-leg internal coolant passages of gas turbine airfoils with film-cooling hole ejection, ASME J. Turbomach. 124 (2002) 499–507.

[16] Editorial Board of ASME Journal of Heat Transfer, Journal of heat transfer policy on reporting uncertainties in experimental measurements and results, ASME J. Heat Transfer 115 (1993) 5–6.

[17] G. Rau, M. Çakan, D. Moeller, T. Arts, The effect of periodic ribs on the local aerodynamic and heat transfer performance of a straight cooling channel, ASME J. Turbomach. 120 (1998) 368–375.

[18] X. Gao, B. Sundén, Heat transfer and pressure-drop measurements in rib-roughened rectangular ducts, Exp. Therm. Fluid Sci. 24 (2001) 25–34.

[19] F.W. Dittus, L.M.K. Boelter, University of California, Berkeley, CA, Publications in Engineering 2 (1930) 443.7.